The current issue and full text archive of this journal is available at
www.emeraldinsight.com/0264-4401.htm

Three-dimensional modelling of bond behaviour between concrete and FRP reinforcement

Valentina Salomoni, Gianluca Mazzucco, Carlo Pellegrino and Carmelo Majorana
Department of Structural and Transportation Engineering, University of Padua, Padua, Italy

Received 20 March 2009
Revised 1 December 2009, 30 March 2010
Accepted 8 April 2010

Abstract

Purpose – The purpose of this paper is to investigate the bond behaviour between fiber reinforced polymer (FRP) sheets and concrete elements, starting from available experimental evidences, through a calibrated and upgraded 3D mathematical-numerical model.

Design/methodology/approach – The complex mechanism of debonding/peeling failure of FRP reinforcement is studied within the context of damage mechanics to appropriately catch transversal effects and developing a more realistic and comprehensive study of the delamination process. The FE ABAQUS© code has been supplemented with a numerical procedure accounting for Mazars's damage law inside the contact algorithm.

Findings – It has been shown that such an approach is able to catch the delamination evolution during loading processes as well.

Originality/value – A Drucker-Prager constitutive law is adopted for concrete whereas FRP elements are assumed to behave in a linear-elastic manner, possibly undertaking large strains/displacements. Surface-to-surface contact conditions have been applied between FRP and adjacent concrete, including the enhancement given by the strain-softening law according to Mazars' damage model. The procedure has been introduced to describe the coupled behaviour between concrete, FRP and adhesive resulting in specific bonding-debonding features under different load levels.

Keywords Polymers, Concretes, Bonding, Modelling

Paper type Research paper

Nomenclature

A	= Mazars' material parameter	F	= failure surface
B	= Mazars' material parameter	g	= gap function
D	= damage variable	g_N	= gap function in normal direction
D^{n+1}	= damage variable at step (n + 1)	g_{Tk}	= gap function in tangential direction k (k = 2, 3)
d	= cohesion		
ε_f	= strain in FRP	g_{0i}	= initial gap function along i direction (i = 1, 2, 3)
ε_c	= strain in concrete		
$\mathbf{e}$	= strain vector	$\mathbf{I}$	= identity matrix
$\mathbf{e}_i$	= strain vector along i direction	l_f	= FRP sheet length
$\mathbf{e}_i^{n+1}$	= strain vector along i direction at step (n + 1)	K_0	= initial value of the softening parameter in Mazars' law
E_f	= FRP elastic modulus	k	= material parameter for Drucker-Prager model
E_{ii}	= elastic coefficient along ii direction		
E_0	= elastic modulus for virgin material	k_f	= FRP stiffness

Engineering Computations: International Journal for Computer-Aided Engineering and Software
Vol. 28 No. 1, 2011
pp. 5-29

0264-4401
DOI 10.1108/02644401111096993

$\mathbf{n}$ = normal vector
n_f = numbers of FRP layers
$\mathbf{n}^j$ = normal vector at point j
$P_{u,exp}$ = experimental ultimate limit load
$P_{u,num}$ = numerical ultimate limit load
p = hydrostatic stress
q = von Mises equivalent stress
r = third invariant of deviatoric stress
$\mathbf{t}$ = stress vector
$\mathbf{t}_i^j$ = stress vector at point j along i direction
$\mathbf{t}_i^{n+1}$ = stress vector along i direction at step (n + 1)
$\bar{\mathbf{t}}^1$ = stress vector at point $\bar{\mathbf{x}}^1$
$\mathbf{t}^2$ = stress vector at point $\mathbf{x}^2$
t_f = FRP thickness
$\mathbf{S}$ = deviator stress tensor
s = slip
$\bar{s}$ = deviator stress measure
$\mathbf{x}^i$ = position vector at node i
z_i = position of strain gauge i

Greek letters

β = friction angle
$\boldsymbol{\varepsilon}$ = strain tensor
ε_0 = limit linear elastic strain
$\bar{\varepsilon}$ = maximum strain value
ε_i^s = deformation in correspondence of strain gauge i
Δg_i = gap function variation along i direction
Δg_i^{n+1} = gap function variation along i direction at step (n + 1)
Γ^i = external surface of body i
Γ^c = contact surface/contact zone
Ω^i = body i
$\boldsymbol{\sigma}$ = stress tensor
$\tilde{\sigma}$ = effective stress tensor
σ = average stress for 1D problem
σ_f = axial stress on the FRP sheet
τ = shear stress along delamination direction

1. Introduction

The last two decades have seen a significant interest in the use of fiber reinforced polymers (FRPs) for civil engineering structures including bridges, buildings, parking garages and residential constructions. On one side, their use has been driven by the desire to find non-corroding reinforcing materials alternative to steel and, on the other, for the purposes of developing cost effective and durable structural strengthening and rehabilitation solutions. FRPs are applied both in internal applications like ordinary steel bars in concrete and for external applications in the form of wraps, laminates or sprays applied for repair and strengthening of steel, concrete and timber structures. In the case of repair and strengthening, in spite of the ever-increasing use of FRPs in civil construction, the bond developed between FRP and the substrate material remains not fully cleared. Very little is understood of the mechanisms that allows bonding to be developed, particularly long-term and cyclic bond behaviour.

Externally bonded FRP sheets are currently used to repair and strengthen existing reinforced concrete (RC) structures for shear (Pellegrino and Modena, 2002, 2006, 2008) and flexural (Pellegrino and Modena, 2009a; Valluzzi *et al.*, 2009) applications: an important issue is proper design against various debonding failure modes (Pellegrino *et al.*, 2008; Lu *et al.*, 2005; Taljsten, 1997; Bizindavyi and Neale, 1999; Chen and Teng, 2001; Nakaba *et al.*, 2001), including cover separation, plate end interfacial debonding (mode 1), intermediate flexural crack-induced interfacial debonding (mode 2), and critical diagonal crack-induced interfacial debonding (mode 3) defined in (Consiglio Nazionale delle Ricerche (CNR), 2004). Therefore, the behaviour of the interface between FRP and concrete support is one of the main elements controlling debonding failures in RC structures strengthened with FRP sheets/plates. The most common failure modes are shown in Figure 1, i.e. the intermediate flexural crack-induced interfacial debonding (mode 2), the case studied in this work, in flexural strengthening applications. The tests shown in Figure 1 have been developed at the University of Padua, Italy.

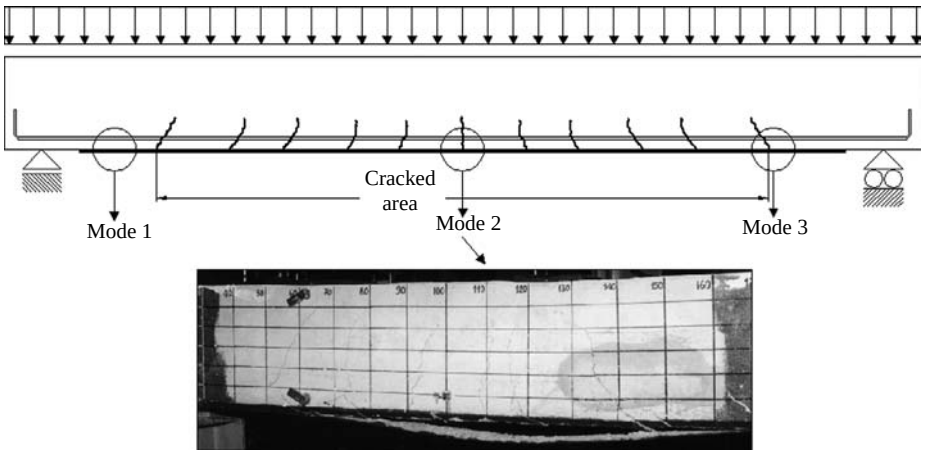

Figure 1.
Failure modes involving delamination at concrete-FRP interface

Additionally, delamination between FRP and concrete in the anchorage zone causes very brittle fracture mechanisms. This phenomenon depends on many factors, e.g. load level, concrete characteristics, rigidity of adhesive and FRP plate.

Therefore, even if many experimental and analytical studies have been undertaken to understand the bond behaviour between FRP and substrate, its current comprehension is generally limited to semi-empirical two-dimensional approaches (Leung *et al.*, 2006a; Savoia *et al.*, 2003; Pellegrino and Modena, 2009b). In Ferracuti *et al.* (2006) and Ferretti and Savoia (2003), a non-linear two-dimensional behaviour is attributed to the interface and the solution is reached via a finite differences scheme; in Point and Sacco (1996), Bruno and Greco (2001), Bruno *et al.* (2003, 2006, 2007) and Greco *et al.* (2007) the two-dimensional interface model is based on fracture and contact mechanics and on the evaluation of the energy release rate. A non-linear softening phenomenological curve is used in Leung *et al.* (2006b) and Rabinovitch and Frostig (2001) whereas in Hormann *et al.* (2002) fracture energies are used as control parameters but the adhesive layer is not taken into account.

First examples of 3D modelling of bond behaviour can be found in Kishi *et al.* (2005), where a smeared-crack approach is followed and the relation between bonding stress and relative displacements has been defined according to the European Committee for Concrete-International Federation for Prestressing model code, and in Riccio and Pietropaoli (2008) where delamination buckling and growth have been analyzed on composite plates. The first demonstration that the stress distribution is significantly different from plane stress assumption can be found in Chen and Pan (2006).

The present work proposes to investigate the bond behaviour between FRP sheets (of various types and amounts) and concrete elements, starting from already available experimental evidences to appropriately calibrate the mathematical-numerical model chosen for the simulation of the above phenomena, within a three-dimensional domain (Chen and Pan, 2006). In this way, transversal effects can be caught and allow for a more realistic and comprehensive study of the delamination process.

Particularly, it is here proposed to study the complex mechanism of debonding/peeling failure of FRP reinforcements within the context of damage

mechanics, appropriately enhancing the potentialities of the finite element (FE) code ABAQUS©, which allows for developing geometric non-linear and changing-status analyses, by supplementing it with a numerical procedure accounting for Mazars's damage law inside the contact algorithm. It will be shown that such an approach is able to catch delamination and its evolution during the loading process by means of the comparison between numerical and experimental results developed at the University of Padua, Italy (Pellegrino *et al.*, 2008).

2. Numerical modelling of delamination processes

The loss of adhesion between FRP and concrete may concern both laminates or sheets applied to RC beams as flexural and/or shear strengthening. Cracks in such strengthened structures may occur within concrete, between concrete and adhesive, adhesive and FRP, within adhesive or FRP.

A realistic numerical modelling of debonding within a FE context requires to implement damage laws in the contact conditions, being the contact algorithm alone not sufficient to catch the triggering of delamination and its evolution. Indeed, the contact method is characterized by the conditions of contact or no-contact but the behaviour in the transition state is generally treated with a Coulomb friction procedure, hence getting a softening response is not possible. Again, the necessity of developing an upgraded contact procedure to model bonding-debonding processes is supported by experimental evidences, as reported in the following.

When a proper installation is adopted, as the adhesive strength is typically much higher than the concrete tensile strength, debonding always takes place within concrete itself with the removal of a thin layer of material (CNR, 2004). Hence, concrete cracking usually occurs in the superficial zone close to the interface only: this cracking due to debonding has been taken into account in the numerical model by means of the contact-damage model at the interface.

2.1 Contact conditions

The interaction between concrete and FRP plates can be described through contact algorithms. In a FE analysis contact conditions are a special class of discontinuous constraints allowing forces to be transmitted from one part of the model to another. The constraint is discontinuous because it is applied only when the two surfaces are in contact. When the two surfaces are separated, the constraint is not applied.

If bodies Ω^1 and Ω^2 are in contact, there are two surfaces Γ^1 in body Ω^1 and Γ^2 in body Ω^2 in contact, and the contact zone $\Gamma^C = \Gamma^1 \cap \Gamma^2$ is defined (Figure 2).

Numerically, contact surfaces are created from the element faces. In this study, the body Ω^1 is the FRP sheet where the contact surface Γ^1 is defined as the master surface and concrete (body Ω^2) is defined as Γ^2, the slave surface.

In the contact zone Γ^c the non-penetration condition must hold:

$$(\mathbf{x}^2 - \bar{\mathbf{x}}^1) \cdot \mathbf{n}_1 \geq 0 \quad on\, \Gamma^c \tag{1}$$

where $\bar{\mathbf{x}}^1$ is a point of Ω^1 with minimum distance from $\mathbf{x}^2$.

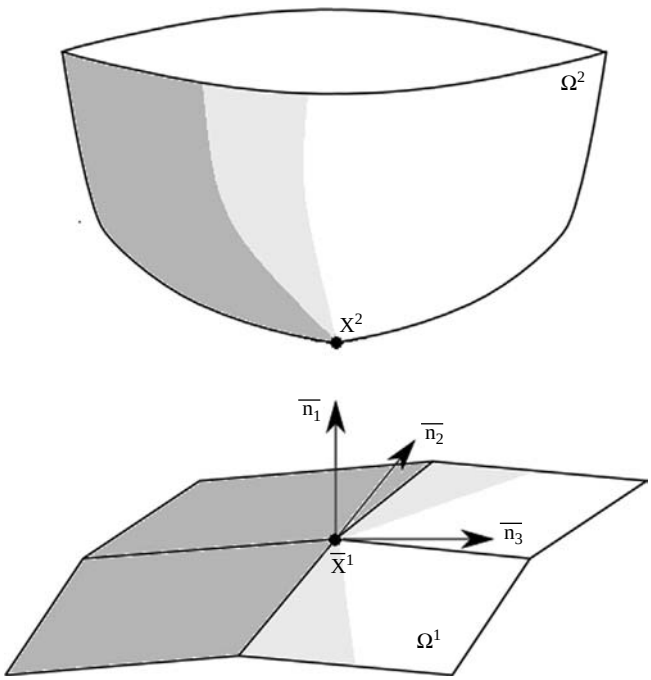

Figure 2.
Contact condition

The gap functions are defined by Belytschko *et al.* (2001) and Wriggers (2006):

$$\begin{aligned} g_N &= (\mathbf{x}^2 - \bar{\mathbf{x}}^1)\cdot\mathbf{n}_1 \\ g_{Tk} &= (\mathbf{x}^2 - \bar{\mathbf{x}}^1)\cdot\mathbf{n}_k \end{aligned} \tag{2}$$

where g_N is the gap in normal direction and g_{Ti} are the tangential gaps in k direction, k = 2, 3.

The equilibrium condition on Γ^c is written through the action-reaction condition:

$$\mathbf{t}^2 - \bar{\mathbf{t}}^1 = 0 \quad on\,\Gamma^c \tag{3}$$

where $\mathbf{t}^j$ is the stress vector at the point j. If we consider the Cauchy stress tensor $\boldsymbol{\sigma}$, the vector $\mathbf{t}^j$ is given by:

$$\mathbf{t}^j = \boldsymbol{\sigma}\mathbf{n}^j \tag{4}$$

We can define three components of the stress vector $\mathbf{t} = (\mathbf{t}_1, \mathbf{t}_2, \mathbf{t}_3)$ according to the local orthonormal reference system $(\mathbf{n}_1, \mathbf{n}_2, \mathbf{n}_3)$, see Figure 3:

$$\begin{aligned} \|\mathbf{t}_1\| = \|\mathbf{t}_N\| = \mathbf{t}\cdot\mathbf{n}_1 \Rightarrow \mathbf{t}_1 = \|\mathbf{t}_1\|\mathbf{n}_1 \\ \mathbf{t}_T = \mathbf{t} - \mathbf{t}_N = (\mathbf{t}_2, \mathbf{t}_3); \mathbf{t}_2 = (\mathbf{t}_T\cdot\mathbf{n}_2)\mathbf{n}_2; \mathbf{t}_3 = (\mathbf{t}_T\cdot\mathbf{n}_3)\mathbf{n}_3 \end{aligned} \tag{5}$$

The strain vector $\mathbf{e} = (\mathbf{e}_1, \mathbf{e}_2, \mathbf{e}_3)$ is defined by:

$$\begin{aligned} \mathbf{e} &= \boldsymbol{\varepsilon}\mathbf{n} \\ \mathbf{e}_1 = (\mathbf{e}\cdot\mathbf{n}_1)\mathbf{n}_1; \mathbf{e}_2 &= [(\mathbf{e} - \mathbf{e}_1)\cdot\mathbf{n}_2]\mathbf{n}_2; \mathbf{e}_3 = [(\mathbf{e} - \mathbf{e}_1)\cdot\mathbf{n}_3]\mathbf{n}_3 \end{aligned} \tag{6}$$

where $\boldsymbol{\varepsilon}$ is the strain tensor.

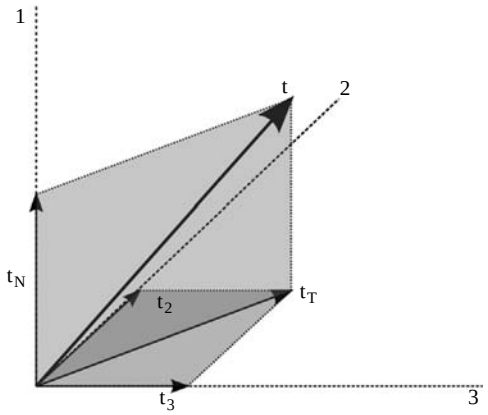

Figure 3.
Stress vector decomposition

In the contact approach the strain vector $\mathbf{e}_i$ can be found by means of increments in relative positions between the two surfaces $\|\mathbf{e}_i\| = \Delta g_i / g_{0i}$ where g_{0i} is the gap function when the analysis starts. A similar approach can be found in Bruno and Greco (2001).

A first assumption allows for relating stress and strain by means of a diagonal matrix (Wriggers, 2006) in a principal reference system:

$$\begin{bmatrix} t_1 \\ t_2 \\ t_3 \end{bmatrix} = \begin{bmatrix} E_{11} & 0 & 0 \\ 0 & E_{22} & 0 \\ 0 & 0 & E_{33} \end{bmatrix} \cdot \begin{bmatrix} e_1 \\ e_2 \\ e_3 \end{bmatrix} \tag{7}$$

where E_{ii} are the constitutive coefficients, $E_{ii} = E_{ii}(D)$, where D is the damage variable.

In the below list the procedure for the numerical implementation of the delamination process is described:

Numerical delamination process
CONTACT CLOSED
STEP n + 1:
1) Calculate
- increments in relative position between the two surfaces Δg_i^{n+1} for all directions
- total deformations e_i^{n+1}

2) Damage check:
IF $|e_i^{n+1}| < \tilde{\varepsilon}$ THEN
$D^{n+1} = D^n$
ELSE
$\tilde{\varepsilon} = |e_i^{n+1}|$
$D^{n+1} =$ see equation (9)
END IF
IF $D^{n+1} \geq 0.9999$ THEN
CONTACT OPEN
end
END IF

3) Evaluate elastic coefficients $E_{ii}^{n+1} = E_0(1 - D^{n+1})$ where E_0 is the elastic modulus of virgin material.
4) Stress vector:

$$\begin{bmatrix} t_1^{n+1} \\ t_2^{n+1} \\ t_3^{n+1} \end{bmatrix} = \begin{bmatrix} E_{11}^{n+1} & 0 & 0 \\ 0 & E_{22}^{n+1} & 0 \\ 0 & 0 & E_{33}^{n+1} \end{bmatrix} \cdot \begin{bmatrix} e_1^{n+1} \\ e_2^{n+1} \\ e_3^{n+1} \end{bmatrix}$$

end

2.2 Mazars' damage law

The Mazars' damage law is usually adopted to evaluate concrete damage. From experimental evidences (Figure 4) the delamination process occurs in the first layer of concrete adjacent to FRP/adhesive. For this reason Mazars' damage model can be applied for studying the debonding effect between FRP and concrete.

An isotropic damage law is here considered and briefly recalled in the following: the effective stress is defined as:

$$\tilde{\sigma} = \frac{\sigma}{1 - D} \tag{8}$$

Figure 4.
Typical delamination occurring in a shear test

for a 1D problem; when D = 0 the material is virgin whereas, when 0 < D <1 the material is affected by damage, up to D=1 corresponding to full damage, i.e. fracture.

The evolution of damage $D = D(\tilde{\varepsilon})$ according to Mazars depends on the strain level and it is given by:

$$D^{n+1} = \begin{cases} 0 & if\ \tilde{\varepsilon} \leq \varepsilon_0 \\ 1 - \frac{(1-A)K_0}{\tilde{\varepsilon}} - \frac{A}{\exp^{(B(\tilde{\varepsilon}-k_0))}} & if\ \tilde{\varepsilon} > \varepsilon_0 \end{cases} \quad (9)$$

The reader is referred to Mazars and Pijaudier-Cabot (1989) and Majorana *et al.* (1998) for additional details.

Damage is an irreversible process and the variable D cannot decrease. In the numerical procedure the damage variable D is defined in the incremental form given by equation (9) and the not-decreasing condition can be seen in "Numerical delamination process" list where the damage variable D is upgraded only if the strain component e^{n+1} at step (n + 1) is larger than $\tilde{\varepsilon}$. In this case $\tilde{\varepsilon} = |e^{n+1}\|$ and D^{n+1} is upgraded with equation (9).

The proposed three-dimensional model is schematically shown in Figure 5 for sake of clarity. In that scheme the elastic-damage behaviour is defined in the contact zone only (with no directional restrictions) where delamination will occur. The FRP is assumed to behave as a linear elastic material, in agreement with the results of experimental tests, whereas a Drucker-Prager model is used to characterize the constitutive behaviour of concrete, as reported below.

The contact-damage model has been implemented using a fortran routine and linked to ABAQUS ("Numerical delamination process"); the subroutine determines the 3D damage at each step and allows for the occurrence of sliding between the contact elements if D is different from zero.

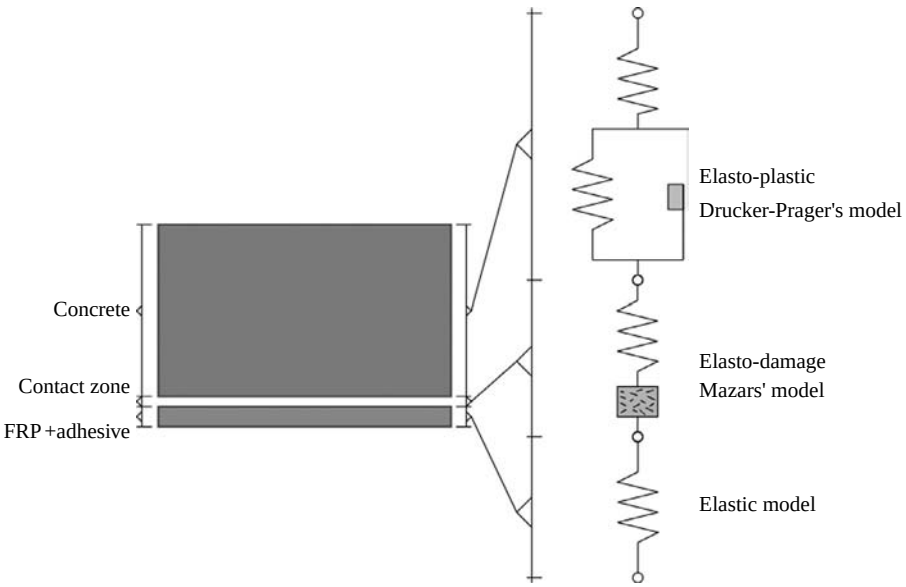

Figure 5.
Schematic of the model and analogical scheme, active along each direction

2.3 Concrete constitutive law

A Drucker-Prager constitutive law has been assumed to model the non-linear behaviour of concrete in compression and in tension, that is computationally efficient. A sensitivity analysis has been additionally performed to check the behaviour of the contact-damage model in the interface zone, as reported in the following.

The failure surface in the (t, p) plane is described by:

$$F = \bar{s} - p \cdot \tan(\beta) - d = 0 \tag{10}$$

where β is the friction angle and d the cohesion. The hydrostatic stress p is determined by:

$$p = \frac{1}{3} tr(\boldsymbol{\sigma}) \tag{11}$$

$\bar{s}$ is the deviator stress measure, defined by:

$$\bar{s} = \frac{q}{2}\left[1 + \frac{1}{k} - \left(1 - \frac{1}{k}\right) \cdot \left(\frac{r}{q}\right)^2\right] \tag{12}$$

where q is the von Mises equivalent stress $q = \sqrt{3/2\,\mathbf{S} : \mathbf{S}}$, **S** the deviator stress tensor $\mathbf{S} = \boldsymbol{\sigma} - q\mathbf{I}$, r the third invariant of the deviator stress $r = 9/2\,\mathbf{SS} : \mathbf{S}$, and k is a material parameter (given by the ratio between the flow stress in triaxial tension and the flow stress in triaxial compression), variable between 0.778 and 1.0.

3. Available experimental data and numerical analyses

The experimental results used to calibrate the numerical model and check its effectiveness have already been published in Pellegrino *et al.* (2008) and are briefly recalled here for reasons of clarity.

The setup of the double shear test (Figure 6) consisted of two concrete prisms $100 \times 100 \times 300\,mm^3$ at a distance of 20 mm one to the other, connected by two carbon FPR strips 50 mm wide and 200 mm long; the load value was measured through a load-transducer connected to the same system used to register strain gauge values, at a loading rate of about 150 N/sec. Effective bond length, maximum bond/shear stress

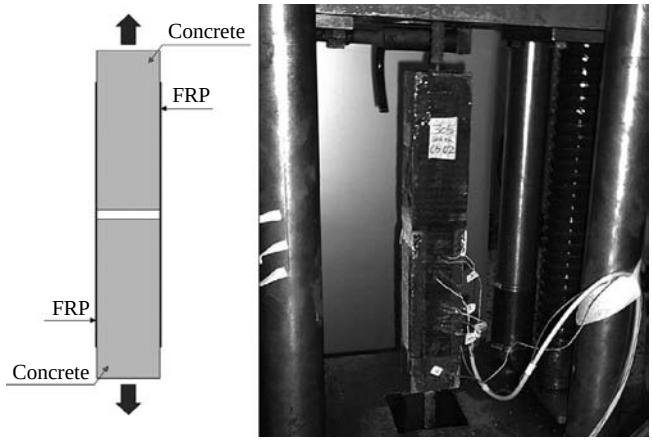

Figure 6.
Double shear test setup

and slip values were experimentally measured and used in Pellegrino *et al.* (2008), Lu *et al.* (2005), Taljsten (1997), Bizindavyi and Neale (1999) and Chen and Teng (2001) to propose new empirical formulas for such parameters, taking into account the influence of FRP stiffness (shear stress refers to the shear component along the longitudinal direction of the specimen). Failure modes were observed and curved fracture lines were detected in a number of specimens; hence the FRP deformation was found to be not constant along the width of the FRP sheet, showing a maximum in the middle of the bonded zone and a minimum at the edges of the FRP strip, as also shown in Figure 17.

This test is representative of post-cracked concrete beams, the ultimate state for the strength of the structure when the FRP fiber only resists to loads. The modelled situation is shown in Figure 7, where the two prisms of concrete are connected by the FRP strip; hence the strip is subjected to traction alone, whereas bending effects are negligible. Hence, such a schematization where the concrete beam is cracked and only the FRP sheet prevents the structure to collapse is reproduced. In fact the scope of the analysis is not to define the triggering and evolution of cracks in concrete (because it is considered that it has already cracked) but to evaluate the ultimate limit load of the structure before complete delamination.

These observations supported the need of developing an appropriate three-dimensional numerical modelling for a better understanding and simulation of the bond behaviour between FRP and concrete. A similar approach has already been followed by Bruno *et al.* (2007) through a smeared-crack model, but the aim was to catch the load-carrying capacity and failure behaviour of RC beams reinforced in flexure with a FRP sheet. In this case, the damaging of the support can represent an important parameter which influences the debonding behaviour and, consequently, the load carrying capacity of the strengthened element and the modelling of the support plays an important role.

The typical double shear test has been reproduced through a 3D model (Figure 8); one-eighth only is represented due to symmetry, characterized by four-noded tetrahedral isoparametric bricks (for the concrete prism) and three-noded triangular isoparametric

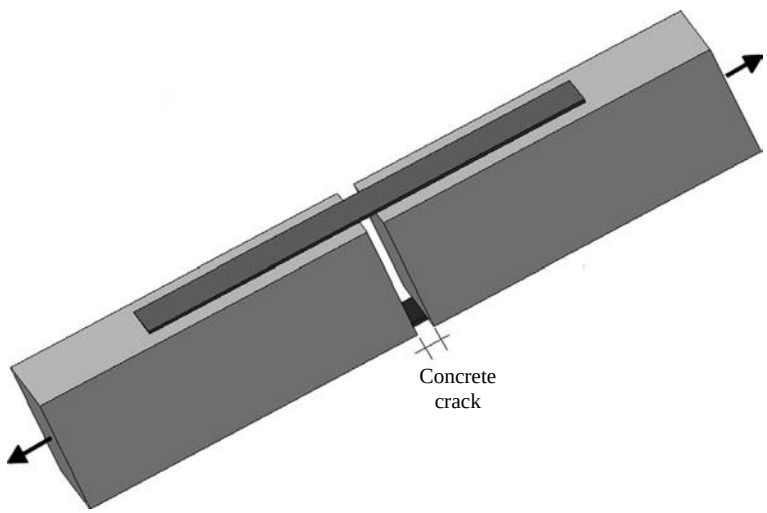

Figure 7.
Test model

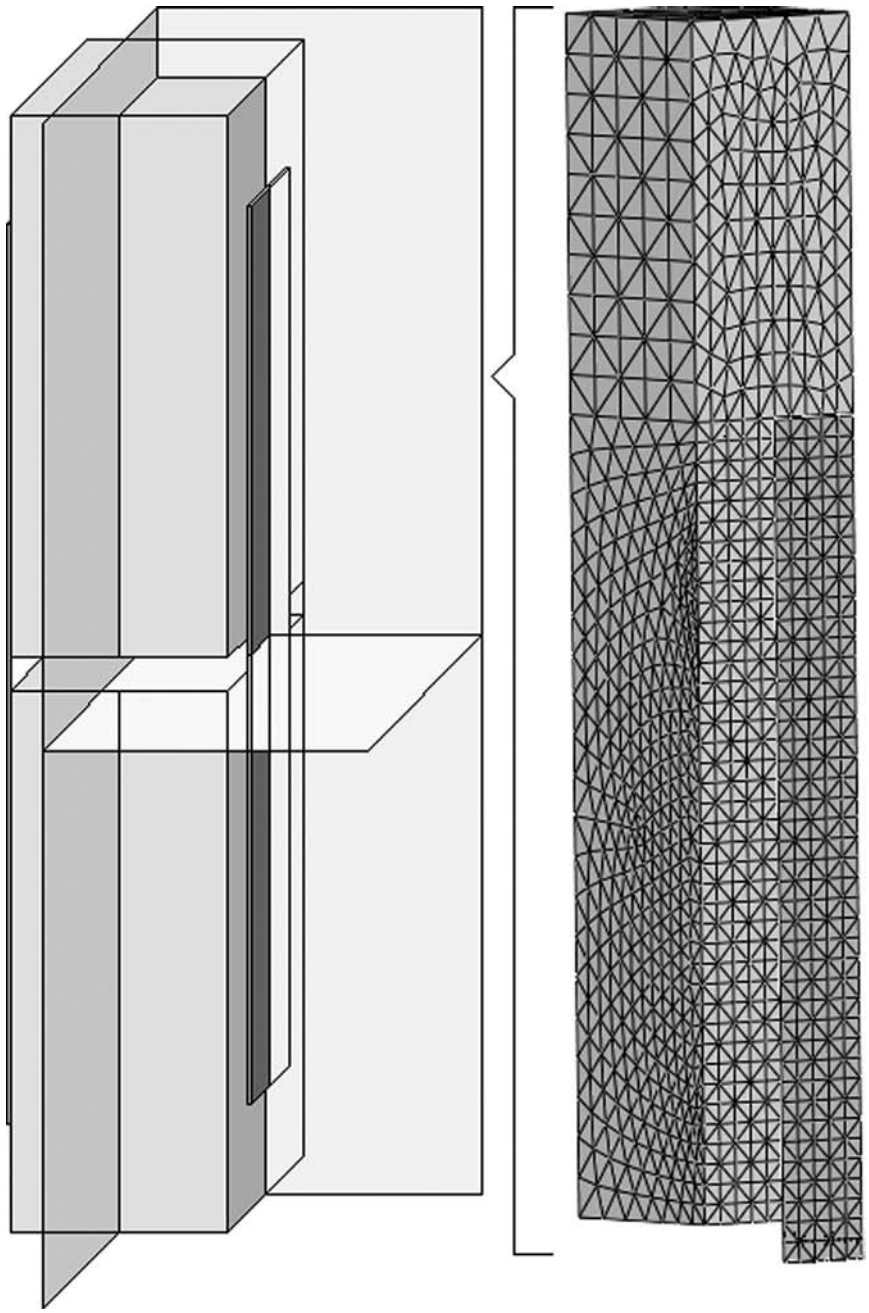

Figure 8.
Adopted discretization and symmetry conditions

plate elements (for the FRP sheet); as stated before, a Drucker-Prager constitutive law is adopted for concrete whereas FRP elements are assumed to behave in a linear-elastic manner, possibly undertaking large strains/displacements. Surface-to-surface contact conditions have been applied between FRP and adjacent concrete including the enhancement given by the strain-softening law according to Mazars' damage model. The procedure has been introduced to describe the coupled behaviour between concrete, FRP and adhesive resulting in specific bonding-debonding features under different load levels.

The undertaken analyses included large deflections and strongly non-linear material effects. A Newton-Raphson iterative solution algorithm with force convergence criterion was used. For each load step an average of ten substeps were applied for reaching equilibrium. On completion of an equilibrium iteration the stiffness matrix was updated for changes in geometry, stress stiffening effects and out-of-balance forces. The total number of run steps was 260, with a minimum load increment of 0.001 per cent and a maximum of 22 per cent of the total load.

The calibration of the Mazars' model has been first developed in agreement with the experimental values of the ultimate loads P_u obtained by previous tests dealing with the same investigation (Pellegrino and Modena, 2002). These specimens have the same geometry but FRP stiffness has been varied by superimposing various FRP layers and by assuming different elastic moduli (Table I). So the Mazars' parameters reported in Table II come directly from such calibration analyses.

Particularly, in Table I n_f is the number of FRP layers, t_f the thickness of one FRP sheet and k_f the FRP stiffness evaluated from the expression $k_f = n_f t_f E_f$;

The adopted material data are listed in Table II.

It is here briefly recalled that the delamination process is characterized by three states under continuous increase in the applied load level: in the first (state 1), cracks start in the

Table I.
Experimental and numerical ultimate loads for calibration analysis

n_f	t_f (mm)	E_f (MPa)	k_f (kN/m)	$P_{u,exp}$ (kN)	$P_{u,num}$ (kN)
1	0.165	390,000	6,435	17.8	17.7
2	0.165	230,000	75,900	21.8	21.0
3	0.165	230,000	113,850	26.4	25.7

Table II.
Material data

	Concrete	FRP	Contact zone
Elastic modulus (MPa)	47,700.0	230,000.0	3,034.0
Poisson's coefficient	0.2	0.3	0.3
Width (mm)	100.0	50.0	–
Height (mm)	100.0	–	–
Length (mm)	600.0	400.0	–
Thickness (mm)	–	0.495	1.1
f_c (MPa)	58.0	–	–
A (Mazars' parameter)	–	–	1.0
B (Mazars' parameter)	–	–	55.0
K_0 (Mazars' parameter)	–	–	0.0012

FRP zone subjected to maximum shear: an increase in traction on the fibers induces an increase in shear stress at the concrete-FRP interface until the stress peak is reached and a micro-debonding occurs; in the second state (state 2) the interface is subjected to both an increase in stress and softening (where a peak has already been reached), so that the stress peak moves from the cracks' triggering point towards the FRP's unloaded part causing a micro-debonding propagation. Under certain load levels, the slip reaches its maximum value and stresses fall to zero, giving rise to the process of macro-debonding. The third state (state 3) refers to complete debonding and the phenomenon eventually propagates in an unstable manner: the final debonding depends on the cracking scheme characterizing the substrate.

As evidenced by Figure 9, up to 40 per cent of the maximum applied load (26 kN), stresses increase nearly linearly (this behaviour can be associated to state 1), then the shear stress peak moves towards the internal part of the FRP and the zone subjected to maximum stress enlarges up to a limit value (state 2) corresponding to 50 per cent of the load. Under further increase in the load level the debonding (state 3) starts and the bond length decreases until the complete detachment between concrete and FRP occurs. The movement of the dark band towards the end of the specimen shows the evolution of the delamination process until complete debonding.

The stress distribution across the FRP plate follows a parabolic-type shape, in agreement with what obtained in the experimental tests (Pellegrino *et al.*, 2008). The stress-strain relationship at the interface (Figure 10, referring to, e.g. the middle point of Figure 18) is typically an elastic-softening one, in agreement with the implemented damage law for the contact algorithm. The descending branch is modified by the A and B parameters provided by Mazars' law.

In the following, the main numerical results are compared with available experimental evidences and they refer to points located in the middle of the FRP sheet; numerical shear stresses (Figure 11; the origin of the abscissa refers to the top of the concrete sample, i.e. the separation zone of Figure 7) decrease more rapidly along the

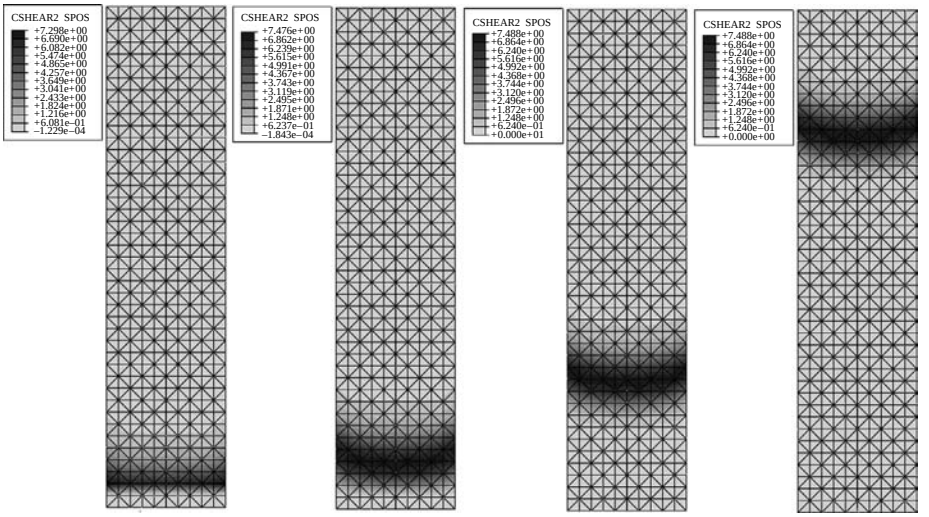

Note: From the left to right contour maps of shear stress under 40, 50, 68, 95 per cent of the maximum load

Figure 9.

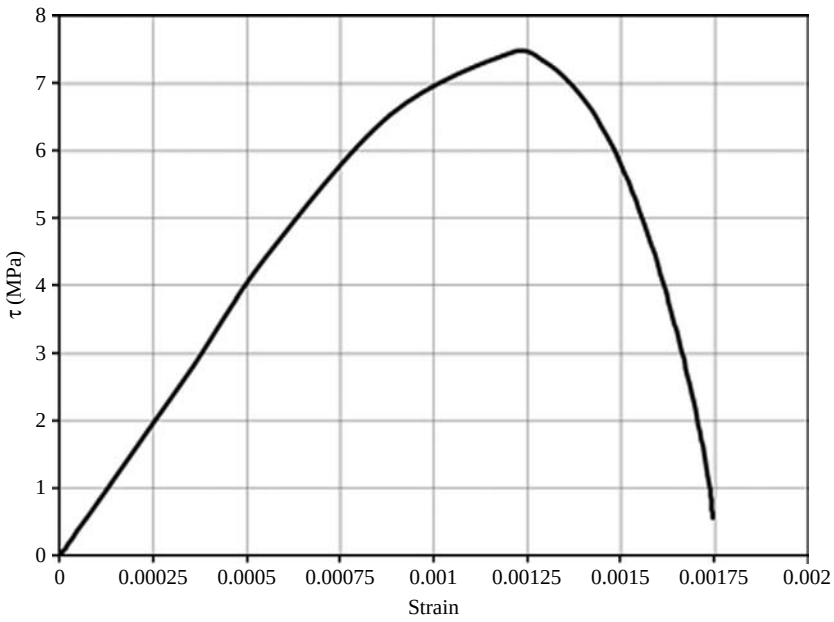

Figure 10.
Numerical stress-strain curve at the contact zone

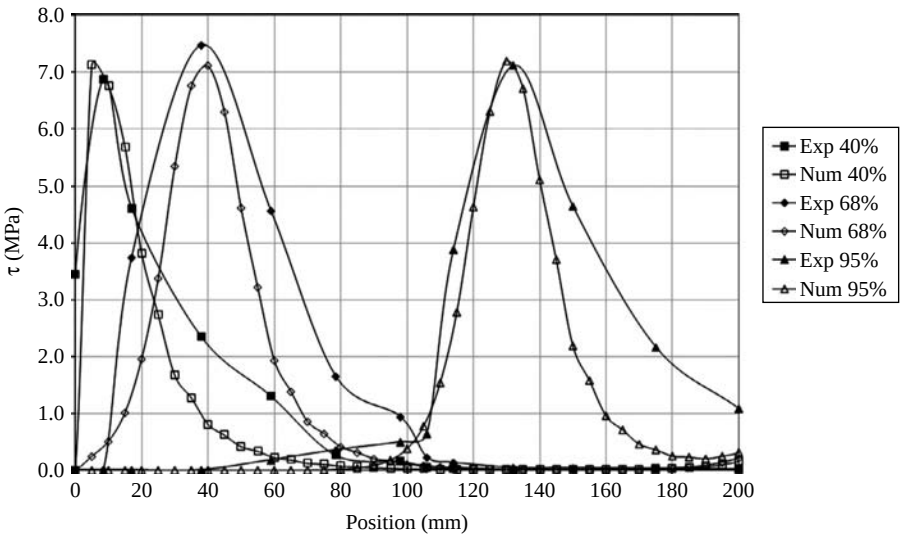

Figure 11.
Numerical and experimental shear stresses vs position under 40, 68 and 95 per cent of the maximum applied load

fiber plate than the experimental ones but both the bonding length (the length along which the bond stress is not zero), the curves' shapes and the peaks are respected.

The ultimate load (100 per cent) corresponds to the situation closest to complete debonding/delamination of FRP from the concrete support (i.e. shear stress equal to zero in the whole bonding zone); clearly, the load reduces to zero when the plate is

completely debonded. When 95 per cent of the ultimate load is reached, the strip is delaminated for a part of its length but still active for the remaining part (Figure 11) to which the effective bond length refers. A further small increase of the applied load (from 95 to 100 per cent) is necessary to approach the complete delamination. The comparison with the experimental test is hence developed when the applied load is 95 per cent of the ultimate load since, in this case, a part of the strip is still active.

A linear elastic behaviour is assumed for the FRP only for the calculation of bond stresses starting from measured strains, as explained below.

Numerical strains (Figure 12) are very close to the experimental values under load levels ranging from 40 per cent (delamination has not started yet) to 68 per cent when debonding is developing. Under the load level close to the ultimate one, the analyses showed deformations stabilized around 0.003 against a maximum experimental peak of 0.004: such a difference (reported also, e.g. by Lu *et al.* (2005)) is simply due to transversal movements of the nearly detached fiber, inducing possible errors (specifically, an overestimation) in the collected experimental values.

The experimental values of bond/shear stress τ are calculated by a simple equilibrium equation of a segment of FRP sheet subjected to axial stresses σ_f and $\sigma_f + d\sigma_f$ and to shear stresses $\tau(z)$ along the length dz of the segment (Pellegrino *et al.*, 2008). Considering discrete distribution of the strain gauges, which are the only locations at which deformation is known, the equation may be written in a discrete manner:

$$\tau(z_i) = \frac{1}{2} n_f t_f E_f \left(\frac{\varepsilon_i^s - \varepsilon_{i-1}^s}{z_i - z_{i-1}} + \frac{\varepsilon_{i+1}^s - \varepsilon_i^s}{z_{i+1} - z_i} \right) \tag{13}$$

where ε_i^s indicates deformation at generic strain gauge i, and z_i its position.

The slip shown in Figure 13 was calculated in agreement with Pellegrino *et al.* (2008), starting by assuming:

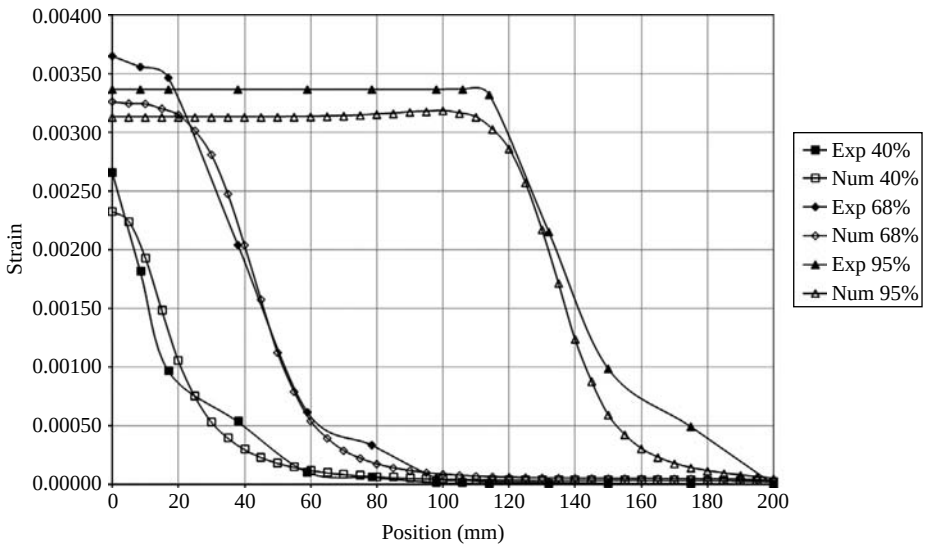

Figure 12. Numerical and experimental deformations vs position under 40, 68 and 95 per cent of the maximum applied load

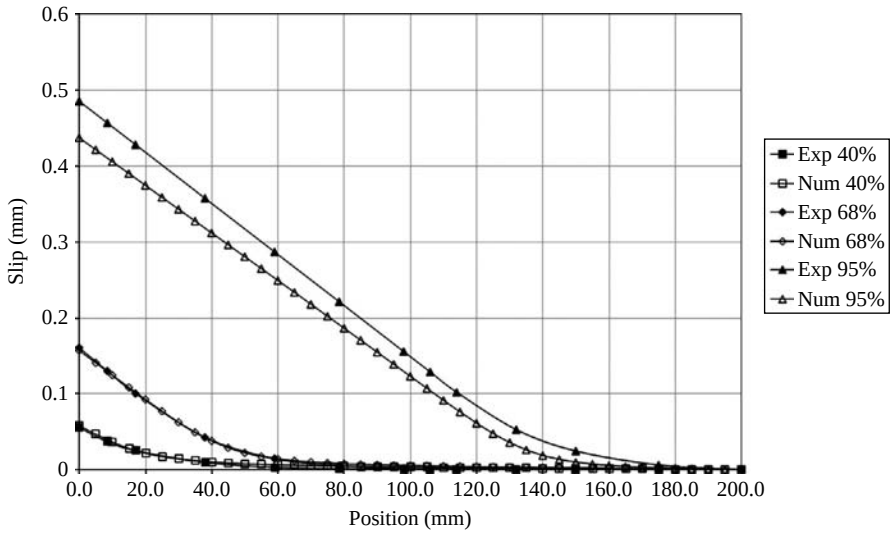

Figure 13.
Numerical and experimental slip vs position under 40, 68 and 95 per cent of the maximum applied load

$$\frac{ds}{dz} = \varepsilon_f - \varepsilon_c \cong \varepsilon_f \tag{14}$$

where concrete deformation ε_c may be neglected with respect to FRP deformation ε_f. Therefore:

$$s(z) = s(0) + \int_0^z \varepsilon_f(\bar{z})d\bar{z} \tag{15}$$

Considering a discrete distribution of strain gauges, the previous equation may rewritten in a discrete manner:

$$s(z_i) = s(l_f) + \sum_{j=n}^{i} \frac{1}{2}(\varepsilon_{j-1} + \varepsilon_j)(z_{j-1} - z_j) \tag{16}$$

where l_f is the total length of the FRP, $s(l_f)$ the slip at the end of the strip and n the total number of strain-gauges. Similarly to what evidenced before, a good agreement is reached up to 68 per cent of the maximum applied load, whereas a shift occurs for higher load levels.

In Figure 14, the comparison between numerical and experimental curves is shown. The method of measuring axial strains by means of closely spaced strain gauges (Lu *et al.*, 2005) cannot produce accurate local bond-slip curves because such strains show violent variations as a result of the discrete nature and the heterogeneity of concrete and the roughness of the underside of the debonded FRP sheet.

Figure 14 is constructed considering, under a given percentage of load level, the shear stress vs slip curve, by taking at any position of the strain gauges (in the experimental test), the value of shear stress and the corresponding slip. In a similar way, we can define shear stress-slip curves considering, now at a fixed point, the load level variation

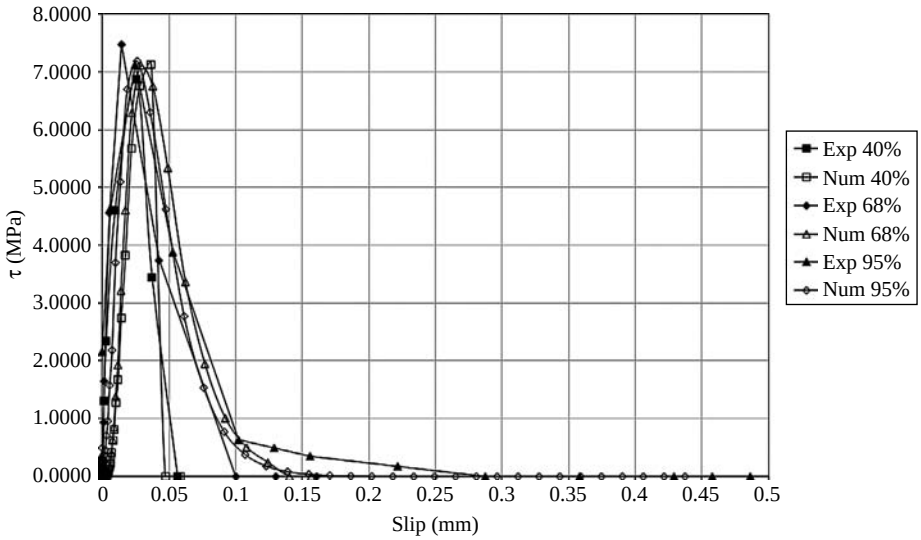

Figure 14.
Shear stress vs slip under 40, 68 and 95 per cent of the maximum applied load

(Figure 15): it is here shown that the global shear stress vs slip behaviour at a certain location is practically the same, but clearly under different load levels.

The shear stress-slip diagram (Figure 15) gives information on the fracture energy, being (CNR, 2004; Savoia *et al.*, 2003; Pellegrino and Modena, 2009b):

$$G = \int_0^{\infty} \tau(s)ds \tag{17}$$

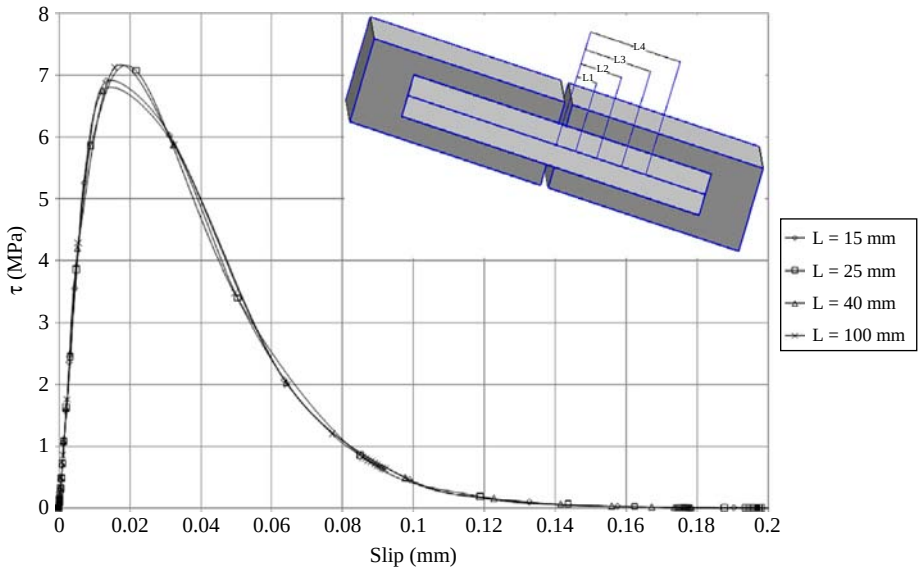

Figure 15.
Numerical shear stress vs slip at a fixed location

Considering a discrete interval of data, the fracture energy takes the form:

$$G_{\max} = \sum_{i=1}^{n} \left[\frac{\tau_{i+1} + \tau_i}{2} \cdot (s_{i+1} - s_i) \right] \tag{18}$$

Equations (17) and (18) correspond to the area under the curve of Figure 15. The variation of energy while the load grows at a fixed position is shown in Figure 16. The maximum value corresponds to the fracture energy defined by equation (18). When $G/G_{max} = 1$ delamination occurs at that point.

As already discussed, such a 3D numerical model was additionally able to catch transversal effects during debonding, in agreement with the experimental results (Figure 17); particularly, the distribution of maximum strain at the interface (i.e. on the FRP-concrete contact surface) follows the crack patterns revealed after rupture of the sample. By taking two reference control points (Figure 18), one in the middle and the other on the edge of the FRP strip, it is possible to evidence (Figure 19) that, under a fixed load level, the deformation at the middle position is higher than at the edge up to sample's collapse; again, during the loading process, the strain curves start diverging until a nearly instantaneous intersection, taking place at end analysis when the FRP has completely debonded.

This means that when using a 2D plane stress state approach, which necessarily assumes a constant stress distribution along the FRP width (not in agreement with experimental evidences), the stress resultants are overestimated; as already evidenced, the maximum stress difference between a middle and an edge point on the FRP is of about 12.5 per cent, hence requiring an adjustment in the FRP's dimension assumed when performing 2D analyses. An equivalent FRP width could be obtained simply through equilibrium conditions for the shear stress resultants (Figure 20):

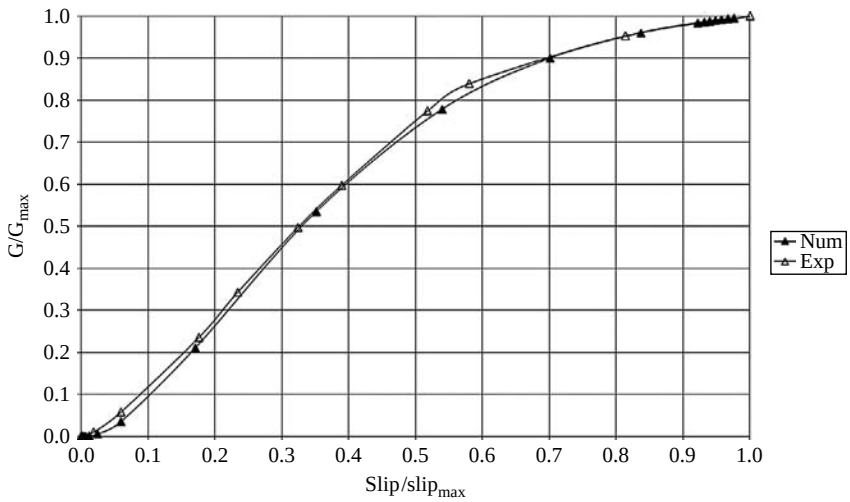

Figure 16.
Energy variation before delamination at position L = 25 mm

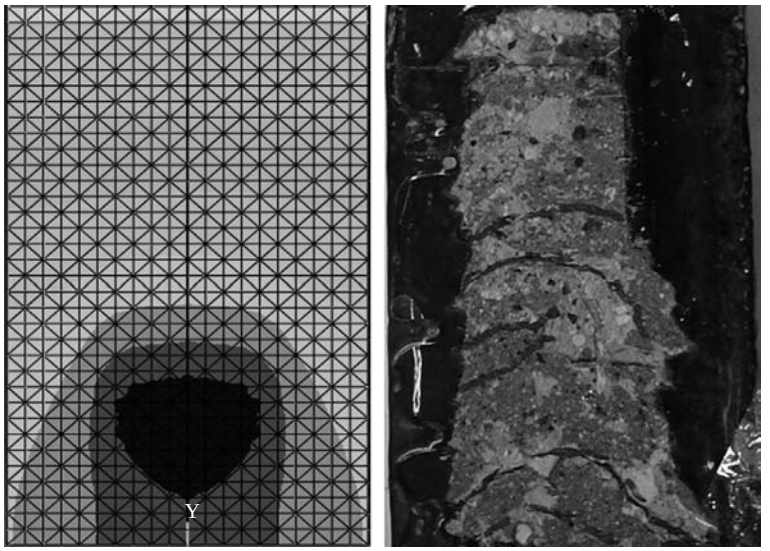

Figure 17.
Numerical and experimental deformation/cracks distribution at the interface at debonding

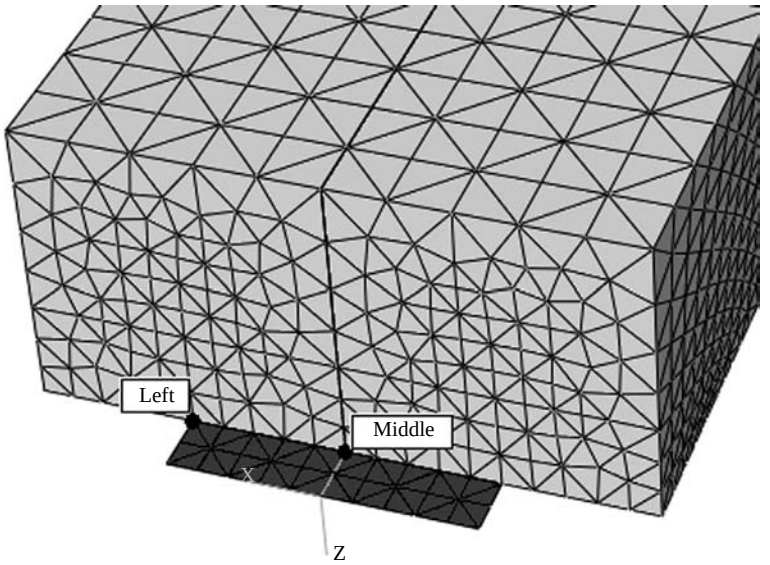

Figure 18.
Control points used for capturing transversal effects

$$\int_0^B \tau ds = \tau_{\max} \cdot B' \tag{19}$$

$$B' = \frac{1}{\tau_{\max}} \int_0^B \tau ds \tag{20}$$

The reduction of the width is estimated, B′/B = 7 per cent.

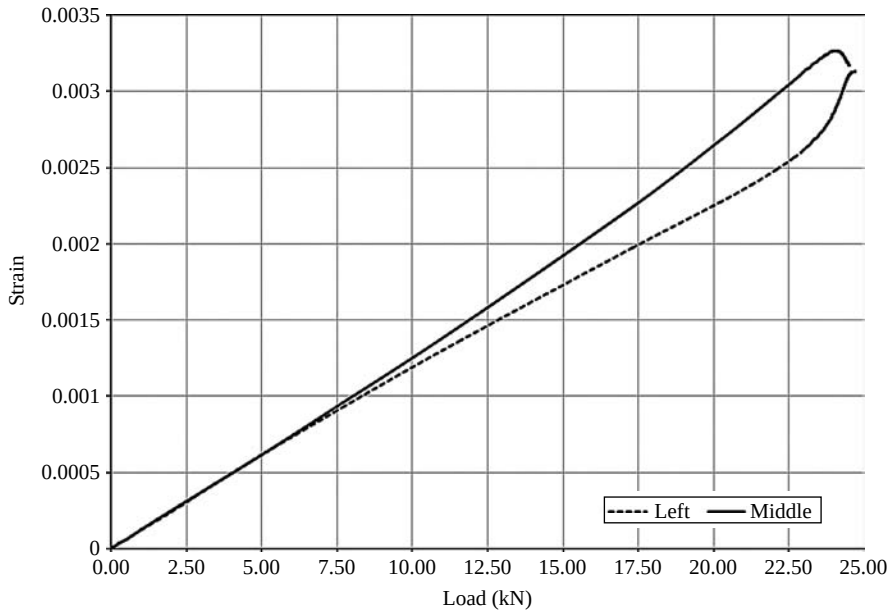

Figure 19.
Strain histories of the control points

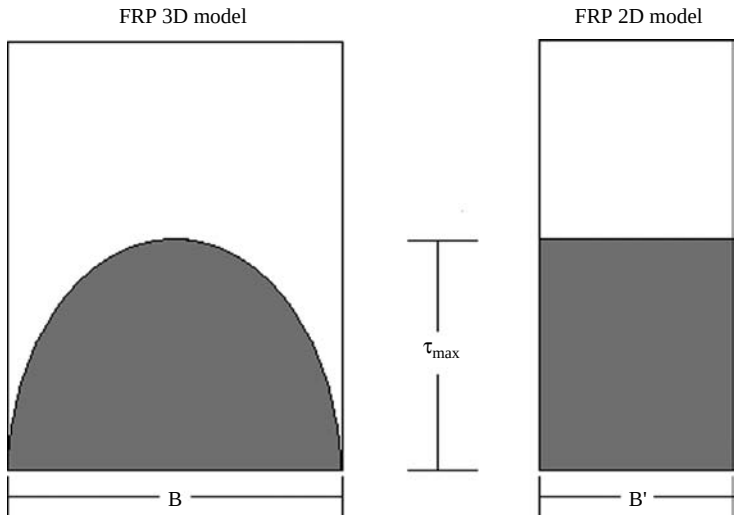

Figure 20.
Integration scheme

The equivalence is clearly valid in considering the peak values only. The integration (in the considered section) has been done when maximum shear stress occurs, so softening has not started yet; hence we are in the elastic limit state and the results are not affected by non-linearities.

4. Mesh sensitivity analysis

To confirm the independence of the numerical results on the mesh at the interface (where the contact-damage model is activated), three discretizations have been characterized as follows (Figure 21):

(1) 4,734 nodes, 20,744 tetrahedral elements and 420 triangular elements.

(2) 7,568 nodes, 5,500 hexahedral elements and 600 quadrilateral elements.

(3) 21,072 nodes, 22,975 hexahedral elements and 1,500 quadrilateral elements.

All the models refer to the same initial/boundary conditions and materials and the comparison has been performed by considering the shear stress distribution in each situation.

The contour maps of Figure 22 shows the shear stress under 50 per cent of the maximum applied load for all discretizations, evidencing the same stress values and 2D distribution. The independence of results on the adopted discretization is confirmed by Figure 23, where the curves of shear stress vs distance (along the FRP strip, in the middle) are reported; just a slight difference in the position of the stress peak for mesh (b) is evidenced, which does not affect the global interfacial behaviour. In Table III, ultimate limit loads are reported for the three models (a), (b) and (c), to further demonstrate the substantial mesh independence on the ultimate load.

5. Conclusions

The bond behaviour between FRP sheets and concrete elements has been here investigated, starting from already available experimental evidences, through a calibrated and upgraded 3D mathematical-numerical model. The system has been viewed as composed by three different physical layers: the concrete base, the adhesive layer and the strengthening bonded FRP strip. The adhesion between layers has been

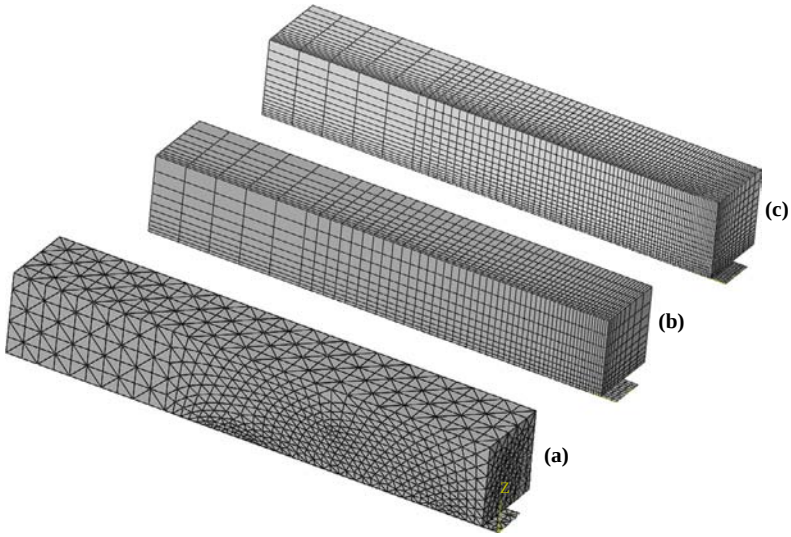

Figure 21.
3D models adopted in the sensitivity analysis

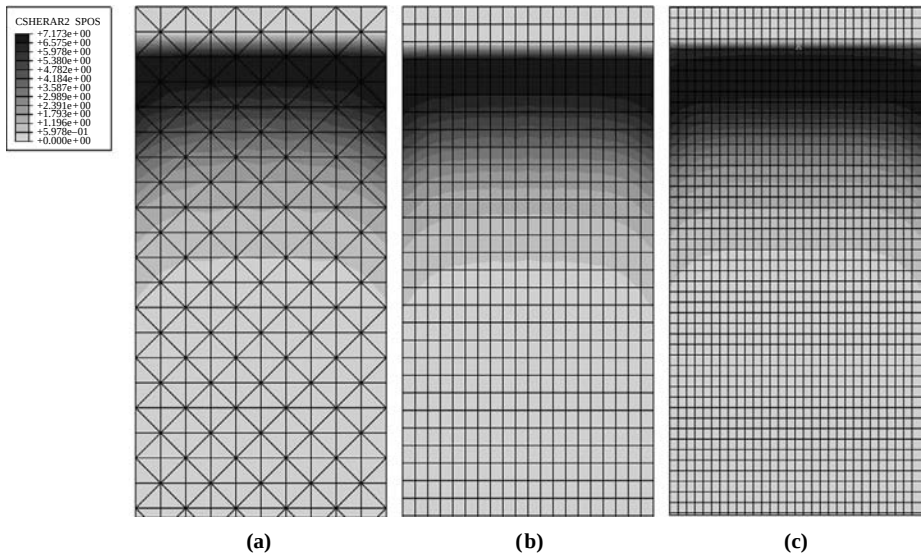

Figure 22.
Contour maps for shear stress under 50 per cent of the maximum load for models (a), (b) and (c)

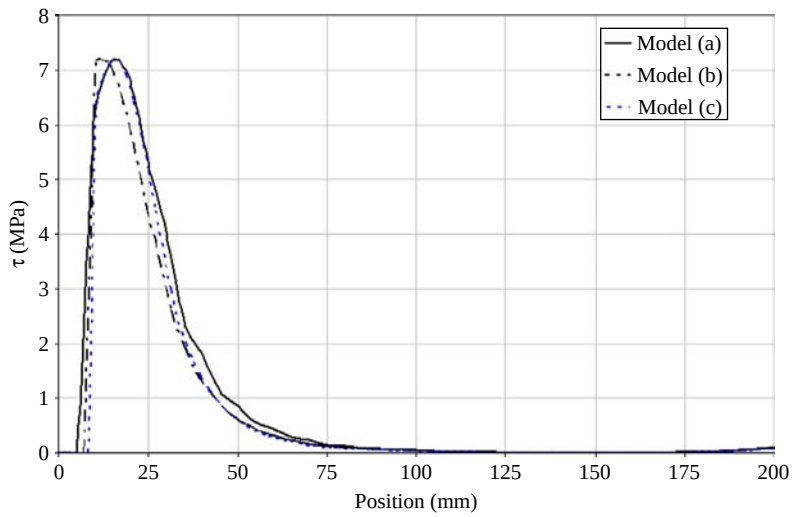

Figure 23.
Shear stress vs distance under 50 per cent of the maximum load for models (a), (b) and (c)

Model	No. of nodes	No. of elements	P_u (kN)
a	4,734	21,164	25.7
b	7,568	6,100	26.0
c	21,072	24,475	25.8

Table III.
Ultimate limit loads for sensitivity analysis

modelled by means of an interface model whose elastic-damage constitutive law relates interlaminar stresses acting in the sliding direction. The FE ABAQUS© code has been supplemented with a numerical procedure accounting for Mazars's damage law inside the contact algorithm. Comparing the numerical results with those of a wide experimental investigation developed at the University of Padua, Italy, in terms of bond stress vs position, axial strain vs position, slip vs position and bond stress vs slip diagrams, it has been shown that such an approach is able to catch delamination from a three-dimensional point of view and its evolution during the entire loading process.

It has been evidenced by such 3D model that FRP deformation is not constant along the transverse axis but has a maximum in the middle of the bonded zone and a minimum at the edges of the FRP strips, confirming experimental evidences and hence demonstrating the suitability of the approach to capture the mechanism of debonding/peeling failure of FRP reinforcements and to catch transversal effects for developing a more realistic and comprehensive study of the delamination process.

The work of the shear tractions acting at the interface through the crack face displacements has been additionally calculated starting from a FD procedure and evaluated under a specified load level.

The practical implications of this study are related to the problem of bond between FRP and concrete, which is the basic phenomenon governing the efficiency of the strengthening technique. Further research will be devoted to 3D numerical simulation of FRP strengthened structural elements (beams and columns) in which debonding/delamination is often the controlling failure mode.

References

Belytschko, T., Liu, W.K. and Moran, B. (2001), *Nonlinear Finite Element for Continua and Structures*, Wiley, Chichester.

Bizindavyi, L. and Neale, K.W. (1999), "Transfer lengths and bond strengths for composites bonded to concrete", *Journal of Composites for Construction*, Vol. 3 No. 4, pp. 153-60.

Bruno, D. and Greco, F. (2001), "Mixed mode delamination in plates: a refined approach", *Int. J. Solids Struct.*, Vol. 38, pp. 9149-77.

Bruno, D., Greco, F. and Lonetti, P. (2003), "A coupled interface-multilayer approach for mixed mode delamination and contact analysis in laminated composites", *Int. J. Solids Struct.*, Vol. 40, pp. 7245-68.

Bruno, D., Carpino, R., Greco, F. and Lonetti, P. (2006), "Energy release rate and mode partition for interlaminar crack in circular laminated beams", *Int. J. Solids Struct.*, Vol. 43, pp. 1201-23.

Bruno, D., Carpino, R. and Greco, F. (2007), "Modelling of mixed mode debonding in externally FRP reinforced beams", *Composites Science and Technology*, Vol. 67, pp. 1459-74.

Chen, J.F. and Pan, W.K. (2006), "Three dimensional stress distribution in FRP-to-concrete bond test specimens", *Construction and Building Materials*, Vol. 20 Nos 1-2, pp. 46-58.

Chen, J.F. and Teng, J.G. (2001), "Anchorage strength models for FRP and steel plates bonded to concrete", *Journal of Structural Engineering*, Vol. 127 No. 7, pp. 784-91.

CNR (2004), "Guide for the design and construction of externally bonded FRP systems for strengthening existing structures: materials, RC and PC structures, masonry structures CNR-DT 200/2004", Italian Research Council, Italian Advisory Committee on Technical Recommendations for Construction, Consiglio Nazionale delle Ricerche, Rome.

Ferracuti, B., Savoia, M. and Mazzotti, C. (2006), "A numerical model for FRP-concrete delamination", *Composites: Part B*, Vol. 37, pp. 356-64.

Ferretti, D. and Savoia, M. (2003), "Non-linear model for RC tensile members strengthened by FRP-plates", *Engineering Fracture Mechanics*, Vol. 70, pp. 1069-83.

Greco, F., Lonetti, P. and Nevone Blasi, P. (2007), "An analytical investigation of debonding problems in beams strengthened using composite plates", *Engineering Fracture Mechanics*, Vol. 74, pp. 346-72.

Hormann, M., Menrath, H. and Ramm, E. (2002), "Numerical investigation of fiber reinforced polymers poststrengthened concrete slabs", *Journal of Engineering Mechanics*, Vol. 128 No. 5, pp. 552-61.

Kishi, N., Zhang, G. and Mikami, H. (2005), "Numerical cracking and debonding analysis of RC beams reinforced with FRP sheet", *Journal of Composites for Construction*, Vol. 9 No. 6, pp. 507-14.

Leung, C.K.Y., Asce, M., Ng, M.Y.M. and Luk, H.C.Y. (2006a), "Empirical approach for determining ultimate FRP strain in FRP-strengthened concrete beams", *Journal of Composite for Construction*, Vol. 10 No. 2, pp. 125-38.

Leung, C.K.Y., Klenke, M., Tung, W.K. and Luk, H.C.Y. (2006b), "Determination of nonlinear softening behaviour at FRP composite/concrete interface", *Journal of Engineering Mechanics*, Vol. 132 No. 5, pp. 498-508.

Lu, X.Z., Teng, J.G., Ye, L.P. and Jiang, J.J. (2005), "Bond-slip models for FRP sheets/plates bonded to concrete", *Engineering Structures*, Vol. 27, pp. 920-37.

Majorana, C.E., Salomoni, V. and Schrefler, B.A. (1998), "Hygrothermal and mechanical model of concrete at high temperature", *Materials and Structures*, Vol. 31, pp. 378-86.

Mazars, J. and Pijaudier-Cabot, G. (1989), "Continuum damage theory – application to concrete", *Journal of Engineering Mechanics*, Vol. 115 No. 2, pp. 345-65.

Nakaba, K., Kanakubo, T., Furuta, T. and Yoshizawa, H. (2001), "Bond behaviour between fiber-reinforced polymer laminates and concrete", *ACI Structural Journal*, Vol. 98 No. 3, pp. 359-67.

Pellegrino, C. and Modena, C. (2002), "FRP shear strengthening of RC beams with transverse steel reinforcement", *Journal of Composites for Construction*, Vol. 6 No. 2, pp. 104-11.

Pellegrino, C. and Modena, C. (2006), "FRP shear strengthening of RC beams: experimental study and analytical modeling", *ACI Structural Journal*, Vol. 103 No. 5, pp. 720-8.

Pellegrino, C. and Modena, C. (2008), "An experimentally based analytical model for shear capacity of FRP strengthened reinforced concrete beams", *Mechanics of Composite Materials*, Vol. 44 No. 3, pp. 231-44.

Pellegrino, C. and Modena, C. (2009a), "Flexural strengthening of real-scale RC and PRC beams with end-anchored pretensioned laminates", *ACI Structural Journal*, Vol. 106 No. 3, pp. 319-28.

Pellegrino, C. and Modena, C. (2009b), "Influence of FRP axial rigidity on FRP-concrete bond behaviour: an analytical study", *Advances in Structural Engineering*, Vol. 12 No. 5, pp. 639-49.

Pellegrino, C., Tinazzi, D. and Modena, C. (2008), "Experimental study on bond behaviour between concrete and FRP reinforcement", *ASCE Journal of Composites for Construction*, Vol. 12 No. 2, pp. 180-9.

Point, N. and Sacco, E. (1996), "A delamination model for laminated composites", *Int. J. Solids Struct.*, Vol. 33 No. 4, pp. 483-509.

Rabinovitch, O. and Frostig, Y. (2001), "Nonlinear high-order analysis of cracked RC beam strengthened with FRP strips", *Structural Engineering*, Vol. 127 No. 4, pp. 381-9.

Riccio, A. and Pietropaoli, E. (2008), "Modeling damage propagation in composite plates with embedded delamination under compressive load", *Journal of Composite Materials*, Vol. 42, pp. 1309-35.

Savoia, M., Ferracuti, B. and Mazzotti, C. (2003), "Non linear bond-slip law for FRP-concrete interface", in Tan, K.H. (Ed.), *FRPRCS-6 Conference Proceedings, Singapore*, pp. 1-10.

Taljsten, B. (1997), "Defining anchor lengths of steel and CFRP plates bonded to concrete", *International Journal Adhesion and Adhesives*, Vol. 17 No. 4, pp. 319-27.

Valluzzi, M.R., Grinzato, E., Pellegrino, C. and Modena, C. (2009), "IR thermography for interface analysis of FRP laminates externally bonded to RC beams", *Materials and Structures*, Vol. 42 No. 1, pp. 25-34.

Wriggers, P. (2006), *Computational Contact Mechanics*, Springer, Berlin.

Corresponding author
Valentina Salomoni can be contacted at: salomoni@dic.unipd.it